*Astronomy & Astrophysics* manuscript no. lindkvist_energy-conversion
May 30, 2018
©ESO 2018

# Energy conversion in cometary atmospheres

## Hybrid modeling of 67P/Churyumov-Gerasimenko

J. Lindkvist[1], M. Hamrin[1], H. Gunell[2,1], H. Nilsson[3], C. Simon Wedlund[4], E. Kallio[5], I. Mann[6], T. Pitkänen[1], and T. Karlsson[7]

[1] Umeå University, Department of Physics, Umeå, Sweden
e-mail: jesper.lindkvist@umu.se
[2] Royal Belgian Institute for Space Aeronomy (BIRA-IASB), Brussels, Belgium
[3] Swedish Institute of Space Physics, Kiruna, Sweden
[4] University of Oslo, Department of Physics, Oslo, Norway
[5] Aalto University, Department of Electronics and Nanoengineering, Espoo, Finland
[6] University of Tromsø, Department of Physics and Technology, Tromsø, Norway
[7] KTH Royal Institute of Technology, School of Electrical Engineering, Stockholm, Sweden

Received DD Month YYYY / Accepted DD Month YYYY

**ABSTRACT**

*Aims.* We want to investigate the energy conversion between particles and electromagnetic fields and where it occurs in the plasma environment of comets.
*Methods.* We use a hybrid plasma model which includes photoionization and we consider two cases of the solar EUV flux. Other parameters correspond to the conditions of comet 67P/Churyumov-Gerasimenko at a heliocentric distance of 1.5 AU.
*Results.* We find that a shock-like structure is formed upstream of the comet and acts as an electromagnetic generator, similar to the bow shock at Earth, slowing down the solar wind. The Poynting flux transports electromagnetic energy towards the inner coma, where newly born cometary ions are accelerated. Upstream of the shock-like structure, we find local energy transfer from solar wind ions to cometary ions. We show that mass loading can be a local process with direct transfer of energy, but also part of a dynamo system with electromagnetic generators and loads.
*Conclusions.* The energization of cometary ions is governed by a dynamo system for weak ionization, but changes into a large conversion region with local transfer of energy directly from solar wind protons for high ionization.

**Key words.** Comets: individual: 67P/Churyumov-Gerasimenko - Sun: UV radiation - (Sun:) solar wind - methods: numerical - plasmas - acceleration of particles

## 1. Introduction

Comets show a highly variable interaction with their environments as their distance to the Sun changes. Sublimated and emitted material from the comet forms a neutral cloud that becomes partially ionized by solar extreme ultraviolet (EUV) radiation and other processes. Far from the Sun, the solar wind impacts directly onto the surface of the comet nucleus in an asteroid-like interaction, while at smaller heliospheric distances the ionized cometary atmosphere (coma) becomes an obstacle to the solar wind. For high outgassing rates, the coma can become dense enough to form plasma boundaries, creating a cometary magnetosphere (Johnstone et al. 1993; Szegö et al. 2000; Cravens & Gombosi 2004).

These magnetospheres have been observed *in situ* by spacecrafts making flybys at (Giotto, ICE, Vega1, Vega2, Suisei, Deep Space 1) or impacting (Deep Impact, Stardust) comets of varying activities and sizes, e.g., 1P/Halley, 26P/Grigg-Skjellerup, 19P/Borrelly, 21P/Giacobini-Zinner (Neugebauer et al. 1990; Coates & Jones 2009). The Rosetta mission rendezvoused with comet 67P/Churyumov-Gerasimenko, a weakly active Jupiter-family comet, for the first time orbiting a comet throughout its perihelion passage in the years 2014–2016 (Glassmeier et al. 2007). Rosetta made continuous *in situ* observations of the plasma environment with a suite of dedicated five plasma instruments (Carr et al. 2007).

One of the objectives of the Rosetta mission was to understand the formation of boundary structures within the cometary atmosphere, and how they evolve with the comet's activity (Simon Wedlund et al. 2016; Glassmeier 2017). The cometary atmosphere becomes ionized by EUV radiation, and locally mass-loads the solar wind. These particles, consisting mostly of water-group ions, are accelerated by the solar wind convective electric field, transferring energy and momentum from the solar wind to the coma. As momentum is transferred to the newly ionized water ions, the solar wind protons deflect in the opposite direction. For weak mass loading, when the ambient electromagnetic fields are mostly undisturbed, modeling shows that water ions will accelerate along the solar wind electric field and E-cross-B drift with a gyroradius much larger than the water ion source region (Kallio & Jarvinen 2012; Lindkvist et al. 2017). The picked up electrons, however, have a gyroradius much smaller than the source region and will therefore behave more fluidlike. Charge separation between electrons and cometary ions will occur (Nilsson et al. 2015b; Behar et al. 2016b). This charge separation could build up a self-polarization of the coma for low activity

comets in the same way as that of a plasmoid penetrating a magnetic barrier (Brenning et al. 1991; Brenning et al. 2005).

Energy will be exchanged from the solar wind particles to the cometary ions via the electromagnetic fields. The energy budget of an interaction can be seen from the Poynting theorem, which describes the conservation of electromagnetic energy, which when neglecting the displacement current is given by

$$\frac{\partial}{\partial t}\left(\frac{B^2}{2\,\mu_0}\right) = -\left(\nabla \cdot \mathbf{S} + \mathbf{E} \cdot \mathbf{J}\right), \tag{1}$$

where $B = |\mathbf{B}|$ is the magnetic field magnitude, and $\mathbf{S} = \mathbf{E} \times \mathbf{B}/\mu_0$ is the Poynting flux, with $\mu_0$ as the permeability of vacuum. The left-hand side of Eq. 1 describes the change of electromagnetic energy density over time, and is zero at steady state. At steady state, the power density (rate of work done by the electric field) is balanced by the divergence of the Poynting flux (the transfer of electromagnetic energy to or from that region).

Energy transfer in magnetized plasmas has been studied at Earth's magnetospheres (also at Venus by, e.g., Saunders & Russell 1986) by looking at the power density, $P = \mathbf{E} \cdot \mathbf{J}$, where $\mathbf{E}$ is the electric field, and $\mathbf{J}$ the current density. The power density is the rate at which the electromagnetic fields do work on charged particles. A generator, $\mathbf{E} \cdot \mathbf{J} < 0$, stores energy in the fields, while a load, $\mathbf{E} \cdot \mathbf{J} > 0$, transfers energy to particles. In the Earth's magnetosphere, loads and generators have been identified in the magnetotail plasma sheet (Hamrin et al. 2011) as well as in the regions along the magnetopause (Rosenqvist et al. 2008). Earth's bow shock drives subsolar reconnection on the dayside magnetopause for southward interplanetary magnetic field (IMF) (Siebert & Siscoe 2002), acting as a generator and slowing down the solar wind flow. Identifying similar regions at comets will tell us where energy dispersion takes place.

Hybrid plasma models are adequate tools to resolve the heavy ion kinetics in the cometary atmospheres. The draping of the magnetic fields and investigation of the diamagnetic cavity has been investigated by, e.g., Koenders et al. (2015). Later, Simon Wedlund et al. (2016) used hybrid models to study the effect that different processes (e.g., charge exchange with solar wind helium) have on the size and shape of the cometary atmosphere. Comparisons between magnetohydrodynamics models (MHD) and hybrid models show distinctive shortcomings in MHD when modeling a weak comet (Rubin et al. 2014), due to not being able to resolve the extremely large gyroradius of the cometary ions. In the hybrid approximation, the electron motion is averaged over one gyroperiod, thus not resolving wave phenomena at the electron scales.

In this paper, we use a hybrid model to study the energy transfer between particles and electromagnetic fields for comet 67P/Churyumov-Gerasimenko (67P). We consider the conditions at the heliocentric distance 1.5 AU (when 67P was at the orbit of Mars) for two extreme conditions of solar EUV radiation. We isolate and identify the regions of energy conversion in the cometary atmosphere, and compare the two cases.

## 2. Model

To model the interaction between the comet 67P and the solar wind plasma, we use a self-consistent hybrid plasma model where we include the production of cometary ions. In the hybrid approximation, ions are treated as particles, and electrons as a massless charge-neutralizing fluid. Below we present the governing equations for the solver and the comet model. See Holmström (2010, 2013) for more information about the solver.

The trajectory of a particle, $\mathbf{r}(t)$ and $\mathbf{v}(t)$, with charge $q$ and mass $m$, is given by the solution of the equation of motion with the Lorentz force, $\mathbf{F}$:

$$\frac{d\mathbf{r}}{dt} = \mathbf{v}, \quad \frac{d\mathbf{v}}{dt} = \frac{\mathbf{F}}{m} = \frac{q}{m}\left(\mathbf{E} + \mathbf{v} \times \mathbf{B} - \eta\mathbf{J}\right), \tag{2}$$

where $\mathbf{E} = \mathbf{E}(\mathbf{r}, t)$ is the electric field, $\mathbf{B} = \mathbf{B}(\mathbf{r}, t)$ is the magnetic field, $\eta$ is the resistivity, and $\mathbf{J} = \mu_0^{-1}\nabla \times \mathbf{B}$ is the current density from the radiation-free Ampère's law (Darwin limit). The resistive term, $\eta\mathbf{J}$, is used as a tool to dampen numerical oscillations in the electromagnetic fields of the collisionless plasma, and is removed in the Lorentz force to prohibit the electron fluid from transferring momentum to the ions (Bagdonat and Motschmann 2002).

The electric field is calculated from the electron momentum conservation equation assuming quasi-neutrality and massless electrons, resulting in Ohm's law:

$$\mathbf{E} = \frac{1}{\rho_\mathrm{i}}\left(-\mathbf{J}_\mathrm{i} \times \mathbf{B} + \mathbf{J} \times \mathbf{B} - \nabla p_\mathrm{e}\right) + \eta\mathbf{J}, \tag{3}$$

where $\rho_\mathrm{i}$ is the ion charge density, $\mathbf{J}_\mathrm{i}$ is the ion current density, $p_\mathrm{e}$ is the electron pressure, and $\eta$ is the resistivity. The electron current, $\mathbf{J}_\mathrm{e}$, is known at all times as $\mathbf{J}_\mathrm{e} = \mathbf{J} - \mathbf{J}_\mathrm{i}$.

The gradient of the electron pressure is calculated by imposing quasi-neutrality and a polytropic index, $\gamma_\mathrm{e}$, giving $\nabla p_\mathrm{e} = \gamma_\mathrm{e} k_\mathrm{B} T_e \nabla n_\mathrm{e}$, with the electron temperature as $T_\mathrm{e} = T_{\mathrm{e},0}\,(n_\mathrm{e}/n_0)^{\gamma-1}$. In this study we approximate electrons having adiabatic processes with three degrees of freedom, corresponding to $\gamma_\mathrm{e} = 5/3$. For this study, the electron pressure gradient term in Ohm's law (Eq. 3) is small, but will play a major role close to the comet nucleus for cases of higher activity (water production).

Faraday's law is used to advance the magnetic field in time,

$$\frac{\partial \mathbf{B}}{\partial t} = -\nabla \times \mathbf{E}. \tag{4}$$

In the limit of a physical vacuum, Faraday's law behaves as a diffusion equation with a resistivity going towards infinity (Hewett 1980). In the model, we define vacuum regions as cells where there are not enough simulated particles (macroparticles) for statistical purposes to solve Ohm's law in Eq. 3. In order to numerically solve Ohm's law, we set $1/\rho_\mathrm{i} = 0$ and $\eta = \eta_\mathrm{v}$ in Eq. 3 whenever the charge density in a cell is lower than what corresponds to half a macroparticle. The numerical parameter $\eta_\mathrm{v}$ is the vacuum resistivity, and is chosen as large as possible. Faraday's law is reduced to solving the magnetic diffusion equation,

$$\frac{\partial \mathbf{B}}{\partial t} = \frac{\eta_\mathrm{v}}{\mu_0}\nabla^2\mathbf{B}. \tag{5}$$

A constraint on the time step is being inferred since the field cannot diffuse more than one cell per time step,

$$\Delta t < \frac{\mu_0\,(\Delta x)^2}{2\eta_\mathrm{v}}, \tag{6}$$

where $\Delta t$ is the time step and $\Delta x$ is the cell size. The time step is for moving the particles (ions). The electromagnetic fields can be updated more frequently (subcycled) since it is usually computationally cheaper to update the fields compared to moving all the particles.

For a comet, when neglecting gravity and assuming a constant outflow velocity, the total flux of non-collisional water vapor will be constant through any spherical shell around the nucleus at distance $r$. This is called the Haser model (Haser 1957), and is described below.

The number density of water vapor, $n$, as a function of the distance, $r$, from the comet nucleus is

$$n_{\mathrm{H2O}}(r) = \frac{Q}{4\pi r^2 u}, \tag{7}$$

where $Q$ is the production rate of water vapor, and $u$ is the mean velocity of water vapor in the radial direction. However, if one accounts for losses (mainly due to photodissociation) the flux will decrease exponentially with time, $t = r/u$, as the molecules move outwards from the nucleus, and one gets

$$n_{\mathrm{H2O}}(r) = \frac{Q}{4\pi r^2 u} \exp\left(-\frac{\nu_{\mathrm{d}} r}{u}\right), \tag{8}$$

where $\nu_{\mathrm{d}}$ is the photodestruction rate of water vapor, which includes all possibilities of photodissociation, photoionization, and dissociative photoionization.

The water vapor is ionized at a certain ionization rate, $\nu_{\mathrm{i}}$, creating water ions, $H_2O^+$. The water ion production rate as a function of distance then becomes

$$q_{\mathrm{i}}(r) = \nu_{\mathrm{i}}\, n_{\mathrm{H2O}}(r), \tag{9}$$

where, in the implementation, the number density of water, $n_{\mathrm{H2O}}$, is taken at the center of each grid cell for each time step, generating the prescribed amount of ions at random positions in that cell.

By not considering the neutral daughter molecules of water via photodestruction, the charge density due to cometary ions will be slightly underestimated (see Simon Wedlund et al. 2017).

### 2.1. Coordinate System and Simulation Box

We use a body-centered right-handed coordinate system in the hybrid model. It is centered in the middle of the nucleus of comet 67P. This is the frame in which we expect the system to reach the most steady-state solution keeping the partial time derivative of Poynting's theorem (Eq. 1) close to zero.

The ambient convective electric field is given by $\mathbf{E}_0 = -\mathbf{u}_0 \times \mathbf{B}_0$, where $\mathbf{u}_0$ is the undisturbed solar wind bulk velocity flowing in the negative x direction, and $\mathbf{B}_0$ is the IMF which is initially homogeneous everywhere. We assume that the IMF has a Parker spiral configuration, with components in the xy plane such that the ambient convective electric field is along the z axis.

The simulation domain is given by $-12,000$ km $< x <$ $6,000$ km, $|y| < 12,000$ km, $|z| < 18,000$ km, and the cubic cell size is $\Delta x = 100$ km. Initially, the domain is filled with 8 solar wind proton macroparticles randomly distributed in each cell. The simulations are run for 100 s. The magnetic fields are updated 16 times for each time step, $\Delta t = 8.2 \times 10^{-3}$.

To dampen numerical oscillations we set the plasma resistivity to $\eta_{\mathrm{p}} = 6.8 \times 10^3\ \Omega$ m. We assume a vacuum resistivity of $\eta_{\mathrm{v}} = 5.7 \times 10^5\ \Omega$ m, which is used when solving the diffusion equation of Faraday's law (Eq. 5) for regions of a charge density less than $\rho_{\mathrm{min}} = e\, n_0/16$, where $n_0$ is the ambient solar wind proton/electron number density, and $e$ is the elementary charge. To summarize:

$$\eta = \begin{cases} \eta_{\mathrm{v}}, & \text{for } \rho_{\mathrm{i}} < \rho_{\mathrm{min}}, \\ \eta_{\mathrm{p}}, & \text{otherwise.} \end{cases} \tag{10}$$

**Table 1.** Solar wind conditions and cometary parameters used in the model.

| Parameter | Denotion | Weak EUV | High EUV |
|---|---|---|---|
| Heliocentric dist. | $R$ [AU/AU] | 1.5 | 1.5 |
| SW number dens. | $n_0$ [cm$^{-3}$] | 3.1 | 3.1 |
| SW B-field mag. | $B_0$ [nT] | 3.4 | 3.4 |
| SW Parker angle | $\chi$ [°] | 56 | 56 |
| SW electron temp. | $k_{\mathrm{B}} T_{\mathrm{e},0}$ [eV] | 11 | 11 |
| SW proton temp. | $k_{\mathrm{B}} T_{\mathrm{H}^+,0}$ [eV] | 5.3 | 5.3 |
| SW bulk speed | $u_0$ [km s$^{-1}$] | 430 | 430 |
| Water speed | $u$ [km s$^{-1}$] | 0.7037 | 0.7037 |
| Water prod. rate | $Q$ [$10^{27}$ s$^{-1}$] | 3.2 | 3.2 |
| Water ion. rate | $\eta_{\mathrm{i}}$ [$10^{-6}$ s$^{-1}$] | 0.15 | 0.37 |
| Water destr. rate | $\eta_{\mathrm{d}}$ [$10^{-6}$ s$^{-1}$] | 5.4 | 9.8 |

### 2.2. Physical parameters

To model the change of the solar wind interaction with the comet at the heliocentric distance of 1.5 AU, we use two cases of solar conditions differing only by change in the extreme ultraviolet (EUV) flux. In the first case the conditions are weakly ionizing and in the other case highly ionizing, corresponding to the quiet and active conditions in Huebner and Mukherjee (2015), respectively. These two cases are summarized in Table 1. The Rosetta mission transpired during a weak solar maximum, with low EUV fluxes. In the model we use typical solar wind conditions from Slavin & Holzer (1981) scaled to the heliocentric distance, $R$, of comet 67P. They can be compared with similar cases previously modeled by Behar et al. (2016a).

The water production rate of a comet changes with distance from the Sun. We use a production rates [s$^{-1}$] of $Q = 2.59 \times 10^{28}\, R^{-5.18}$, where $R$ is a unitless parameter given by the heliocentric distance in terms of AU (Hansen et al. 2016). The neutral water vapor expansion speed is observed to be relatively constant around $u = 700$ m s$^{-1}$ (Gulkis et al. 2015), but a more precise formula by Hansen et al. (2016) has been found to be

$$u = [-55.5\, R + 771] \cdot \left[1 + 0.171 \exp\left(-\frac{R - 1.24}{0.13}\right)\right], \tag{11}$$

given in [m s$^{-1}$], based on combined observations from experiments onboard Rosetta during the comet's inbound orbital phase.

Water ions are produced in the simulation according to Eq. 9. For the photoionization and photodestruction rates we use scaled values with heliocentric distances from Huebner and Mukherjee (2015). Quiet solar conditions give a photoionization rate of $\nu_{\mathrm{i,q}} = 3.31 \times 10^{-7}\, R^{-2}$ s$^{-1}$ and a photodestruction rate of $\nu_{\mathrm{d,q}} = 1.206 \times 10^{-5}\, R^{-2}$ s$^{-1}$. Active solar conditions gives a photoionization rate of $\nu_{\mathrm{i,a}} = 8.28 \times 10^{-7}\, R^{-2}$ s$^{-1}$ and a photodestruction rate of $\nu_{\mathrm{d,a}} = 2.203 \times 10^{-5}\, R^{-2}$ s$^{-1}$.

The undisturbed solar wind plasma parameters are a bulk velocity of $u_0 = 430$ km s$^{-1}$ along $-\hat{x}$ (neglecting aberration),

where $\hat{x}$ denotes the unit vector in the x direction. The number density of protons is $n_0 = 7\,R^{-2}$ cm$^{-3}$, and the temperature of protons and electrons are $T_\mathrm{p} = 8 \times 10^4\,R^{-2/3}$ K and $T_\mathrm{e} = 15 \times 10^4\,R^{-1/3}$ K, respectively. The IMF has a magnitude of $6\,R^{-1}\left(R^{-2}/2 + 1/2\right)^{1/2}$ nT, with a Parker spiral angle of $\chi = \arctan(R)$. The proton temperature is used to generate macroparticle protons at the inflow boundary according to a Maxwellian velocity distribution, whereas the electron temperature can be solved at all points in space and it describes the width of the Maxwellian electron fluid velocity distribution. No water ion temperature is given as an initial condition, since macroparticle water ions are generated via Eq. 9.

## 3. Results

We first present an overview of the solar wind interaction with comet 67P/Churyumov-Gerasimenko at a heliocentric distance of 1.5 AU for weakly ionizing conditions and highly ionizing conditions corresponding to the two cases in Table 1. Afterwards we present the energy conversion of the interaction; where and how much energy is transferred between particles and the electromagnetic fields.

### 3.1. Weakly ionizing case

Figure 1a-b shows the magnetic field magnitude in the xz plane, which is perpendicular to the ambient interplanetary magnetic field (IMF), and in the plane of the IMF (xy), respectively. The magnetic field magnitude is normalized to the ambient solar wind value, $B_0 = 3.4$ nT. In Fig. 1a the magnetic field piles up upstream (to the right) of the comet nucleus, and directly downstream of the nucleus. The high concentration of water ions of cometary origin results in the fact that the magnetic field downstream of the comet nucleus is frozen in to the almost stationary plasma and cannot diffuse to relax the field. Several sharp and thin arcs of magnetic field increase can be seen in the lower part of panel (a). The upper part of the same panel has a more diffuse magnetic field increase on a large region. The disturbed solar wind magnetic field forms a cone in the xz plane with a sudden increase (jump) in the magnetic field. We will refer to the jump at the front of the cone as a shock-like structure. As to what exactly this boundary corresponds to can not be investigated further here due to the lack of spatial resolution at the shock-like structure.

In Fig. 1b the magnetic field is shown in the plane of the IMF. The IMF is draping around the comet, forming a shock-like structure. Since the IMF is tilted in a Parker spiral configuration, the upper part of the panel has a quasi-perpendicular shock-like interaction. Multiple arcs of increased magnetic field are seen inside the shock-like structure for $x \lesssim -3 \times 10^3$ km and $y \gtrsim 3{\times}10^3$ km. The lower part of the panel has a quasi-parallel shock-like interaction, making wave propagation and backflow of ions (and electrons) possible at the boundary.

The draped field lines seen as in Fig. 1b are generally referred to as Alfvén wings, which are Alfvén waves propagating along the magnetic field lines away from either a conducting or mass-loading obstacle (Russell et al. 2016). For the simulation parameters of Table 1 one can note that the Alfvén speed of the undisturbed solar wind, $v_\mathrm{A} \approx 42$ km s$^{-1}$, is lower than the magnetosonic wave speed, $v_\mathrm{MS} \approx 67$ km s$^{-1}$. A compressional wave moving perpendicular to the magnetic field is thus expected to move faster than a shear Alfvén wave along the magnetic field. This is the reason why the shock-like structure is a broader cone in Fig. 1a where the magnetic field is pointing into the plane, than the one seen in Fig. 1b where the magnetic field is located in the plane.

Figure 1c-d shows the solar wind proton number density in color normalized to its ambient value, $n_0 = 3.1$ cm$^{-3}$ for two planes perpendicular to the solar wind flow. The cell averaged velocity is shown as a vector field with an arrow length proportional to its magnitude. In Fig. 1e-f, the water ion number density is shown in color, also normalized to the ambient solar wind proton density.

In Fig. 1e the water ions close to the comet nucleus are accelerated by the convective electric field of the solar wind (towards positive $z$). However, the water ion concentration is high enough to considerably alter the local electromagnetic fields, causing the solar wind protons to transfer much of their momentum to the water ions, making the solar wind deflect towards the opposite direction of the electric field (towards negative $z$). This causes the shock-like structure of increased solar wind proton density seen in Fig. 1c, and has been discussed previously by Behar et al. (2016a,b, 2017).

In the upper part of Fig. 1c there is a swirl of solar wind protons traveling downstream. If one investigates the time evolution of the simulations, they show that the comet system does not come to a steady state, but rather has instabilities on the positive $z$ side. The shock-like structure on the lower part of the same panel connects all the way to the comet nucleus, resulting in solar wind being present in the vicinity of the comet nucleus. Several arcs of increased solar wind proton density are present farther downstream, corresponding to the magnetic field increase seen in Fig. 1a. These arcs are seperated by around $\lambda_\mathrm{A} \approx 500$ km. The ion inertial length of protons in the undisturbed solar wind is $\lambda_{\mathrm{H}^+} = 130$ km. Similar arcs are seen in the magnetic field on the top side of Fig. 1b.

In the weak mass loading limit, the water ions have cycloidal trajectories with a large gyroradius ($\sim 2{\times}10^4$ km). It can be seen from the water ion number density in Fig. 1e-f that water is rather transported downstream into the tail. Along the arcs in the lower panel in Fig. 1a there are almost no water ions, showing that the arc structure is due to the solar wind proton dynamics. These arcs are the effect of gyrating solar wind protons and resemble what is known as an overshoot in supercritical collisionless bow shocks, where the magnetic field is oscillating downstream of such a shock (Heppner et al. 1967; Greenstadt et al. 1968; Russell et al. 1982).

### 3.2. Highly ionizing case

Figure 2 shows the same plasma parameters as Fig. 1 but for the highly ionizing case summarized in Table 1. In the lower part of Fig. 2a, showing the magnetic field magnitude in color in the plane of the ambient solar wind electric field, the magnetic field is bunched together in striations, just as was seen earlier for the weakly ionizing case of Fig. 1a. In the upper part of the same panel ($x = 0$, $z = 10^3$ km), the magnetic field is strongly piled up. This is where the water ions and solar wind meet head on. In Fig. 2b, showing the magnetic field magnitude and vector field in the plane of the IMF, the magnetic field is seen draping around the comet, resulting in a current sheet downstream at $y = 0$. The magnetic field magnitude does not drop to zero, and hence no diamagnetic cavity is present in either case.

The solar wind proton number density is shown in color in Fig. 2c-d. The solar wind flows around the comet and is not present at the comet nucleus. Because of this we call the outermost sudden jumps in density and magnetic field strength "a detached shock-like structure", in analogy to the attached shock-

like structure seen in Fig. 1. The observed "shock jump" of $n_{H^+}/n_0 \sim 4$ corresponds to the hypersonic limit shock jump from the Rankine-Hugionot conditions for a polytropic index of $\gamma = 5/3$ (Cravens 1997).

The water ion number density is shown in Fig. 2e-f. An almost spherically symmetric water ion cloud is formed close to the nucleus, in contrast to the weakly ionizing case seen earlier in Fig. 1e-f. In Fig. 2e the ion cloud is seen to be slightly elongated along the ambient solar wind electric field. In Fig. 2f the ion cloud is seen elongated downstream of the comet nucleus, which corresponds to the current sheet mentioned in the magnetic field structure above. The water ion number density color scale is saturated in Fig. 2e-f close to the nucleus; it reaches a maximum value of $40\,n_0$ within the simulation. Here, the water ions are much more numerous than the solar wind protons, and the electric field within the water ion cloud is close to zero (not shown).

The shock-like structure in Fig. 1a-b is shaped like a bow instead of a cone as in the weakly ionizing case seen in Fig. 1a-b. For the highly ionizing case, the part of the water ion cloud that has higher charge densities than the solar wind has a larger extent than the arc seperation distance of $\lambda_A \approx 500$ km. This means that the source of the waves (i.e. the water ion obstacle) cannot be considered point-like in nature, as is the case for a low ionization.

### 3.3. Energy conversion

The energy balance for the electromagnetic fields is described by the Poynting theorem introduced in Eq. 1. Each term of the Poynting theorem is shown in color in Fig. 3 for weakly ionizing conditions, and in Fig. 4 for highly ionizing conditions.

In Fig. 3a-b the power density, $P = \mathbf{E} \cdot \mathbf{J}$, is shown in color, and it is well balanced by the divergence of the Poynting flux, shown in color in Fig. 3c-d, where the Poynting flux vector, $\mathbf{S} = \mathbf{E} \times \mathbf{B}/\mu_0$, is shown as a vector field. It can be seen in Fig. 3e-f that the time derivative of the electromagnetic energy density, $\partial/\partial t(B^2/2\mu_0)$, is small in comparison to the other terms which implies steady state, meaning that the power density is well balanced by the Poynting flux transport. This reasoning also applies to the highly ionizing condition shown in Fig. 4.

The rate of work (or power) done by the electromagnetic fields on a charged particle can be expressed directly from the Lorentz force in Eq. 2 as $\mathbf{F} \cdot \mathbf{v}$. Summing over all ion species '$s$' in a volume gives the rate of energy transferred between electromagnetic energy and kinetic energy for that charged species, and is in the model given by the power density, $P_s = (\mathbf{E} - \eta\mathbf{J}) \cdot \mathbf{J}_s$, where $\mathbf{J}_s = \rho_s \mathbf{u}_s$, with $\rho_s$ being the charge density and $\mathbf{u}_s$ the bulk velocity.

The total power density can be expressed as a sum of the contributions from each ion species, $s$, and the electron fluid,

$$P = P_e + \sum_s P_s, \tag{12}$$

where $P_e$ is the power density for the electron fluid. The electron fluid power density is calculated from the other terms, which is written as

$$P_e = (\mathbf{E} - \eta\mathbf{J}) \cdot \mathbf{J}_e + \eta\mathbf{J}^2, \tag{13}$$

where the first term is non-dissipative, and the second term is dissipative (depends on the numerical resistivity, $\eta$). As mentioned before, the electron current is known at all times, and is given by $\mathbf{J}_e = \mathbf{J} - \mathbf{J}_i$.

The power density for all species including the electrons can be seen in Fig. 5 for weakly ionizing conditions, shown for cuts in the plane perpendicular to the IMF in the upper panels, and for the plane of the IMF in the lower panels. In Fig. 5a-b the power density, $\mathbf{E} \cdot \mathbf{J}$, is shown in color. Shown in (c,d) of the same figure is the power density for the electron fluid, in (e,f) the power density for solar wind protons, and in (g,h) the power density for the cometary water ions.

In Fig. 5a, the shock-like structure at $z < 0$ (in blue) acts as an electromagnetic generator, $\mathbf{E} \cdot \mathbf{J} < 0$, slowing down the solar wind and piling up the magnetic field, resulting in a higher field energy there. Arcs are present downstream of this structure related to secondary acceleration of solar wind protons. The power density depends on the direction of the total current density, which is alternating direction (not shown). The upper part of Fig. 5a does not reach a steady state along the shock-like structure, and has regions where the power density flips sign (e.g., $x = 0, z = 3 \times 10^3$ km). Downstream of the comet nucleus (to the left) around $z = 0$, there is a large load of electromagnetic energy (in red), $\mathbf{E} \cdot \mathbf{J} > 0$, where the water ions are being accelerated. The power density for electrons (not shown), $\mathbf{E} \cdot \mathbf{J}_e$, is close to zero outside the shock-like structure, and relatively low compared to the other power densities elsewhere. In Fig. 5b the electromagnetic generator (in blue) is along the shock-like structure with an electromagnetic load (in red) close to $y = 0$ downstream of the comet nucleus, where most water ions are located (compare with the water ion density in Fig.1f).

The Poynting flux shown as the vector field in Fig. 3c-d transports the electromagnetic energy from the shock-like structure towards $y = 0$ and in the $-\hat{\mathbf{z}}$ direction. Most water ions are being accelerated close to $y = 0$ where $\mathbf{E} \cdot \mathbf{J}_{H2O^+} > 0$. There, the acceleration is acting as an electromagnetic load, $\mathbf{E} \cdot \mathbf{J} > 0$.

By comparing the four panels Fig. 5e-h one sees that the solar wind protons are mostly slowed down along the shock-like structure, $\mathbf{E} \cdot \mathbf{J}_{H^+} < 0$, transferring energy with Poynting flux towards $y = 0$, where most water ions are accelerated, $\mathbf{E} \cdot \mathbf{J}_{H2O^+} > 0$ (red).

The energy conversion for the comet at the heliocentric distance 1.5 AU for highly ionizing conditions can be seen in Fig. 6, with the same figure structure as Fig. 5. The energy transfer regions can be identified in a similar way to the weakly ionizing case, but with major differences. In Fig. 6a-b, the shock-like structure is acting as a generator. Secondary acceleration of protons is present downstream of the shock-like structure, correlating in location with the arcs. However, there is no strong electromagnetic load close to $y = 0$ downstream of the nucleus for this case.

By comparing the four panels in Fig. 6e-h one sees that most energy is transferred locally from solar wind protons to water ions in regions outside the shock-like structure where $\mathbf{E} \cdot \mathbf{J} \approx 0$, but where $\mathbf{E} \cdot \mathbf{J}_{H^+} < 0$ and $\mathbf{E} \cdot \mathbf{J}_{H2O^+} > 0$.

The acceleration of water ions in the highly ionizing case is noted to be more homogeneous compared to the weakly ionizing case, where acceleration was predominantly in the $y = 0$ plane.

### 3.4. Comparison with observations

Observations by the Rosetta spacecraft is the key to understand the model results. In the two cases analyzed in the paper there is a void formed in solar wind particles, a solar wind cavity, just as in the observations reported by Behar et al. (2017); Nilsson et al. (2017). In the weakly ionizing case the solar wind cavity extends

only about 100 km upstream of the nucleus, whereas in the high activity case it is seen at about 500 km distance upstream. The latter is in approximate agreement with observations, as Rosetta was within the solar wind cavity around comet 67P from about mid April 2015 until December 2015. Rosetta did a dayside excursion when at a heliocentric distance of 1.4 AU out to a comet distance of 1500 km, but still did not leave the solar wind cavity. The size of the solar wind cavity must thus have been at least 1500 km, close to perihelion. During the return from the dayside excursion, faint fluxes of solar wind ions were seen during an extreme space-weather event (Edberg et al. 2016), indicating that the solar wind cavity was significantly compressed during the event, enough so that solar wind particles were seen. Thus it seems that Rosetta could have been near the boundary of the solar wind cavity.

Throughout the mission, when the solar wind was observed, it was not apparently shocked, and the energy of the solar wind ions was not significantly changed. At the same time there was a significant deflection of the solar wind ions, resulting from a direct interaction with the local water ions (Behar et al. 2016a,b). This seems to be best captured by the high activity model as well. Our model results imply that the solar wind – comet atmosphere interaction can behave in different ways for different ionization rates. The diffuser more direct interaction of the highly ionizing case, leading also to a large solar wind cavity, is closest to what was observed by instruments on the Rosetta spacecraft at comet 67P. In the model however, photoionization rates may suffer from uncertainties due to the changing nature of the Sun's EUV spectrum. Time-dependent models of the photoionization, in quiet and more extreme conditions, may prove interesting to elucidate the local composition and dynamics of the cometary plasma.

## 4. Summary and Conclusions

Energy conversion has been analyzed at comet 67P/Churyumov-Gerasimenko using a hybrid plasma model at a heliocentric distance of 1.5 AU for two extremes of solar ultraviolet radiation. These two cases correspond to scenarios where in the weakly ionizing case the solar wind can reach the comet nucleus, while this is not true for the highly ionizing case.

The modeling shows that a shock-like structure is formed upstream of the comet, but it is not the traditional bow shock seen at Earth since there is a large region outside the shock structure where energy is transferred locally from solar wind protons to cometary water ions.

For the weakly ionizing case, the shock-like structure acts as an electromagnetic generator, similar to the bow shock at Earth (Lopez et al. 2011), and this is where the solar wind slows down and the protons lose most of their energy to the ambient cometary plasma and electromagnetic fields. The electromagnetic energy is transported with a Poynting flux towards the inner coma, where most of the water ions are accelerated. The highly ionizing case has the same dynamo mechanism, but with most energy being transferred locally from solar wind protons to water ions, upstream of the shock-like structure.

This leads us to speculate that the acceleration of cometary heavy ions can be both a local process with direct transfer of energy, and a dynamo system with generators and loads, depending on the solar activity conditions. For a comet approaching the Sun, acceleration of cometary ions is dominated by local transfer close to the nucleus, which first evolves into a dynamo system, and finally evolves into a large region with local transfer of energy.

*Acknowledgements.* The software used in this work was in part developed by the DOE NNSA-ASC OASCR Flash Center at the University of Chicago. The hybrid solver is part of the openly available FLASH code and can be downloaded from http://flash.uchicago.edu/. The simulation results are available from the corresponding author upon request. This research was conducted using resources provided by the Swedish National Infrastructure for Computing (SNIC) at the High Performance Computing Center North (HPC2N), Umeå University, Sweden. J. Lindkvist and M. Hamrin are funded by the Swedish National Space Board (SNSB project 201/15). H. Gunell was supported by the Belgian Science Policy Office through the Solar-Terrestrial Centre of Excellence, and by PRODEX/ROSETTA/ROSINA PEA 4000107705. H. Nilsson was supported by the Swedish National Space Board under contract 112/13 and by the Swedish Research Council under contract 2015-04187. C. Simon Wedlund is supported by the Research Council of Norway grant No. 240000. I. Mann was supported by the Research Council of Norway grant No. 262941.

## References

Bagdonat, T., & Motschmann, U. 2002, 3D Hybrid Simulation Code Using Curvilinear Coordinates, J. Comp. Phys., 183, 470–485

Behar, E., Lindkvist, J., Nilsson, H., et al. 2016, Mass-loading of the solar wind at 67P/Churyumov-Gerasimenko: Observations and modelling, A&A, 596, A42

Behar, E., Nilsson, H., Stenberg Wieser, G., et al. 2016, Mass loading at 67P/Churyumov-Gerasimenko: a case study, Geophys. Res. Lett., 43, 1411–1418

Behar, E., Nilsson, H., Alho, M., Götz, C., & Tsurutani, B. 2017, The birth and growth of a solar wind cavity around a comet - Rosetta observations, MNRAS, 469, stx1871

Brenning, N., Kelley, M. C., Providakes, J., Stenbaaek-Nielsen, H. C., & Swenson, C. 1991, Barium Swarm: An Ionospheric Alternating Current Generator in CRIT 1, J. Geophys. Res., 96, 9735–9743

Brenning, N., Hurtig, T., & Raadu, M. A. 2005, Conditions for plasmoid penetration across abrupt magnetic barriers, Physics of Plasmas, 12, 012309

Carr, C, Cupido, E. Lee, C. G. Y., et al. 2007, RPC: The Rosetta Plasma Consortium, Space Science Reviews, 128(1–4), 629–647

Coates, A. J., & Jones, G. H. 2009, Plasma environment of Jupiter family comets, Planetary and Space Science, 57, 10, 1175–1191

Cravens, T. E. 1997, Physics of Solar System Plasmas (Cambridge University Press, Cambridge)

Cravens, T. E., & Gombosi, T. I., 2004, Cometary Magnetospheres: A Tutorial, Advances in Space Research, 33, 11, 1968–1976

Edberg, N. J. T., Alho, M., André, M., et al. 2016, CME impact on comet 67P/Churyumov-Gerasimenko, MNRAS, 462, stw2112

Glassmeier, K-H. 2017, Interaction of the solar wind with comets: a Rosetta perspective, Phil. Trans. R. Soc. A, 375, 2097, 20160256

Glassmeier, K-H., Boehnhardt, H., Koschny, D., Kührt, E., & Richter, I. 2007, The Rosetta Mission: Flying Towards the Origin of the Solar System, Space Science Reviews, 128, 1–4, 1–21

Greenstadt, E. W., Green, I. M., Inouye, G. T., et al. 1968, Correlated magnetic field and plasma observations of the earth's bow shock, J. Geophys. Res., 73, 51

Gulkis, S., Allen, M., von Allmen, P., et al. 2015, Subsurface properties and early activity of comet 67P/Churyumov-Gerasimenko, Science, 347(6220), aaa0709

Hamrin, M., Marghitu, O., Norqvist, P., et al. 2011, Energy conversion regions as observed by Cluster in the plasma sheet, J. Geophys. Res., 116, A00K08

Hansen, K. C., Altwegg, K., Berthelier, J.-J., et al. 2016, Evolution of water production of 67P/Churyumov-Gerasimenko: an empirical model and a multi-instrument study, MNRAS, 462, S491–S506

Haser, L. 1957, Distribution d'intensité dans la tête d'une comèt, Bulletin de la Classe des Sciences de l'Académie Royale de Belgique, 43, 740–750

Heppner, J. P., Sugiura, M., Skillman, T. L., Ledley, B. G., & Campbell, M. 1967, OGO-A magnetic field observations, J. Geophys. Res., 72, 5417

Hewett, D. W. 1980, A global method of solving the electron-field equations in a zero-inertia-electron-hybrid plasma simulation code, Journal of Computational Physics, 38, 378–395

Holmström, M. 2010, Hybrid modeling of plasmas, Springer, Proceedings of ENUMATH, the 8th European Conference on Numerical Mathematics and Advanced Applications, 451–458

Holmström, M. 2013, Handling vacuum regions in a hybrid plasma solver, Numerical modeling of space plasma flows, ASP Conference series, 474, 202–207

Huebner, W. F., & Mukherjee, J. 2015, Photoionization and photodissociation rates in solar and blackbody radiation fields, Planet. Space Sci., 106, 11–45

Johnstone, A. D., Coates, A. J., Huddleston, D. E., et al. 1993, Observations of the Solar Wind and Cometary Ions during the Encounter Between Giotto and Comet Grigg-Skjellerup, A&A 273, L1–L4
Kallio, E., & Jarvinen, R. 2012, Kinetic effects on ion escape at Mars and Venus: Hybrid modeling studies, Earth Planets Space, 64(2), 157–163
Koenders, C., Glassmeier, K.-H., Richter, I., Ranocha, H., & Motschmann, U. 2015, Dynamical features and spatial structures of the plasma interaction region of 67P/Churyumov-Gerasimenko and the solar wind, Planet. Space Sci., 105, 101–116
Lindkvist, J., Holmström, M., Fatemi, S., Wieser, M., & Barabash, S. 2017, Ceres interaction with the solar wind, Geophys. Res. Lett., 44(5), 2070–2077
Lopez, R. E., Merkin, V. G., & Lyon, J. G. 2011, The role of the bow shock in solar wind-magnetosphere coupling, Ann. Geophys., 29, 1129–1135
Neugebauer, M., Coates, A. J., Neubauer, F. M. 1990, Comparison of Picked-up Protons and Water Group Ions Upstream of Comet Halley's Bow Shock, J. Geophys. Res., 95(A11), 18745–18753
Nilsson, H., Stenberg Wieser, G., & Behar, E. 2015, Evolution of the ion environment of comet 67p/churyumov-gerasimenko, A&A, 583, A20
Nilsson, H., Stenberg Wieser, G., Behar, E., et al. 2017, Evolution of the ion environment of comet 67P during the Rosetta mission as seen by RPC-ICA, MNRAS, 469, stx1491
Rosenqvist, L., Vaivads, A., Retinò, A., et al. 2008, Modulated reconnection rate and energy conversion at the magnetopause under steady IMF conditions, Geophys. Res. Lett., 35, L08104
Rubin, M., Koenders, C., Altwegg, K., et al. 2014, Plasma environment of a weak comet – Predictions for Comet 67P/Churyumov–Gerasimenko from multifluid-MHD and Hybrid models, Icarus, 242, 38–49
Russell, C. T., Hoppe, M. M., & Livesey, W. A. 1982, Overshoots in planetary bow shocks, Nature, 296, 45–48
Russell, C. T., Luhmann, J. G., & Strangeway, R. J. 2016, Space Physics (Cambridge University Press, Cambridge)
Saunders, M. A., & Russell, C. T. 1986, Average dimension and magnetic structure of the distant Venus magnetotail, J. Geophys. Res., 91(A5), 5589–5604
Siebert, K. D., & Siscoe, G. L. 2002, Dynamo circuits for magnetopause reconnection, J. Geophys. Res., 107(A7), 1095
Simon Wedlund, C., Kallio, E., Alho, M., et al. 2016, The atmosphere of comet 67P/Churyumov-Gerasimenko diagnosed by charge-exchanged solar wind alpha particles, A&A, 587, A154
Simon Wedlund, C., Alho, M., Gronoff, G., et al. 2017, Hybrid modelling of cometary plasma environments I., A&A, 604, A73
Slavin, J. A., & Holzer, R. E. 1981, Solar Wind Flow About the Terrestrial Planets 1., J. Geophys. Res., 86(A13), 11401–11418
Szegö, K., Glassmeier, K.-H., Bingham, R., et al. 2000, Physics of Mass Loaded Plasmas, Space Sci. Rev., 94, 429–671

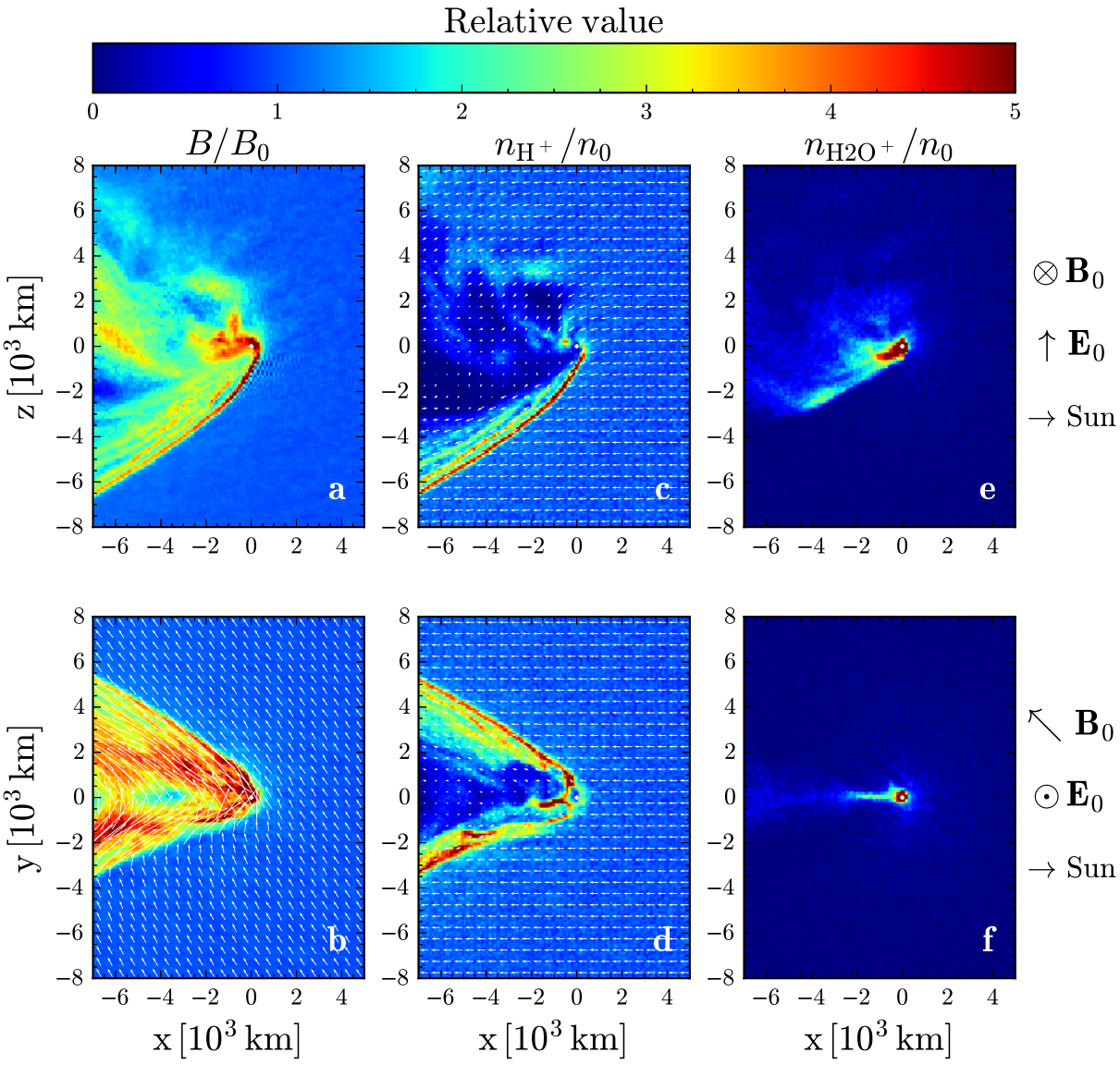


**Fig. 1.** Cuts through the planes $y = 0$ and $z = 0$ for comet 67P at 1.5 AU during weakly ionizing solar conditions. Shown in color of (a, b) is the magnetic field magnitude relative to the ambient solar wind value, $B_0$. The vector field in (b) marks the direction and size of the magnetic field. In (c, d) the color shows the solar wind proton number density relative to its ambient value, $n_0$, and the vector fields mark the velocity of the solar wind protons. In (e, f) the cometary water ion number density relative to the ambient solar wind proton number density. The comet nucleus is marked by white crosshairs. The local geometry for each row of panels is shown to the right of the figure.

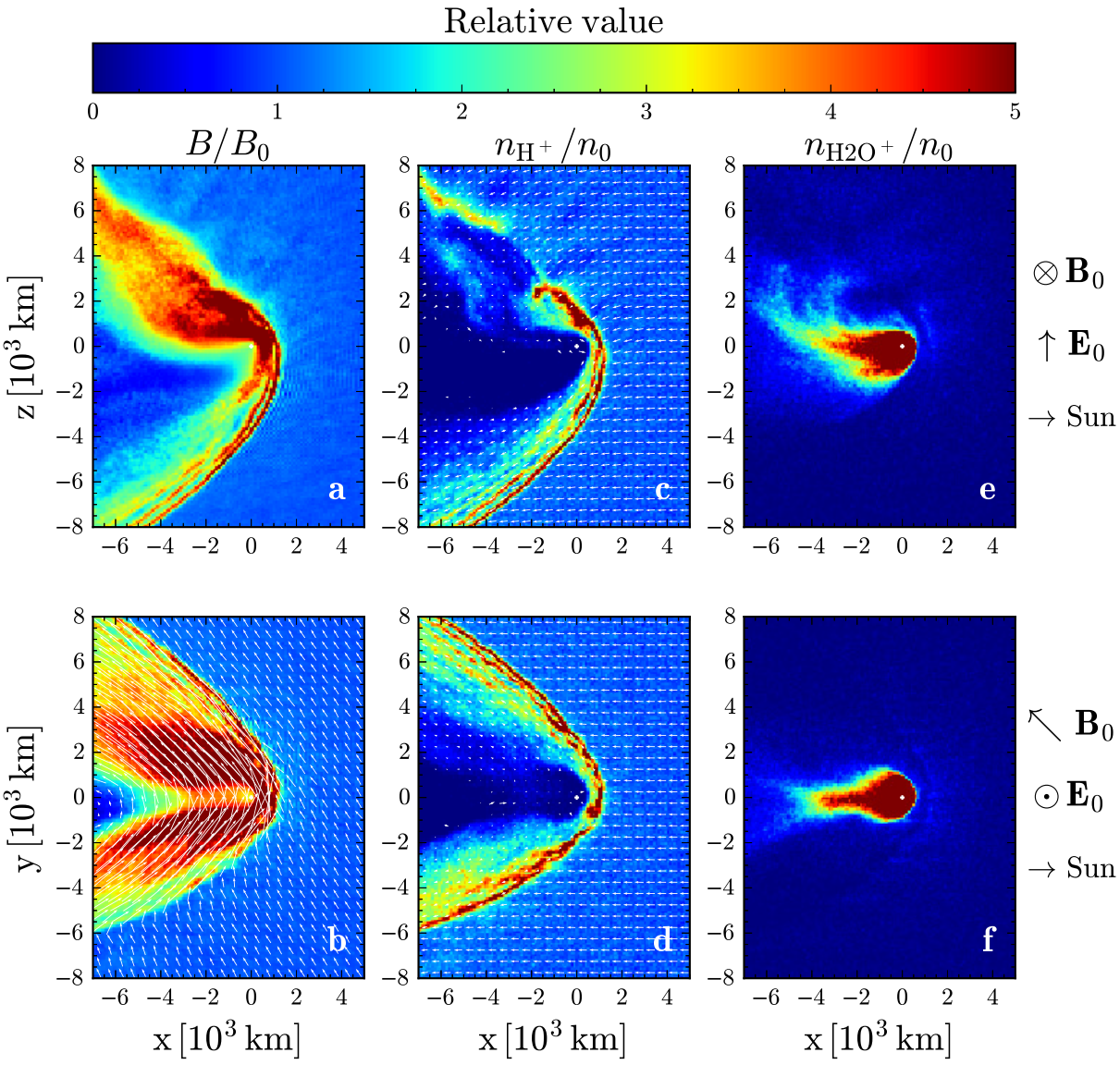


**Fig. 2.** Same form as Fig. 1 but for highly ionizing solar conditions.

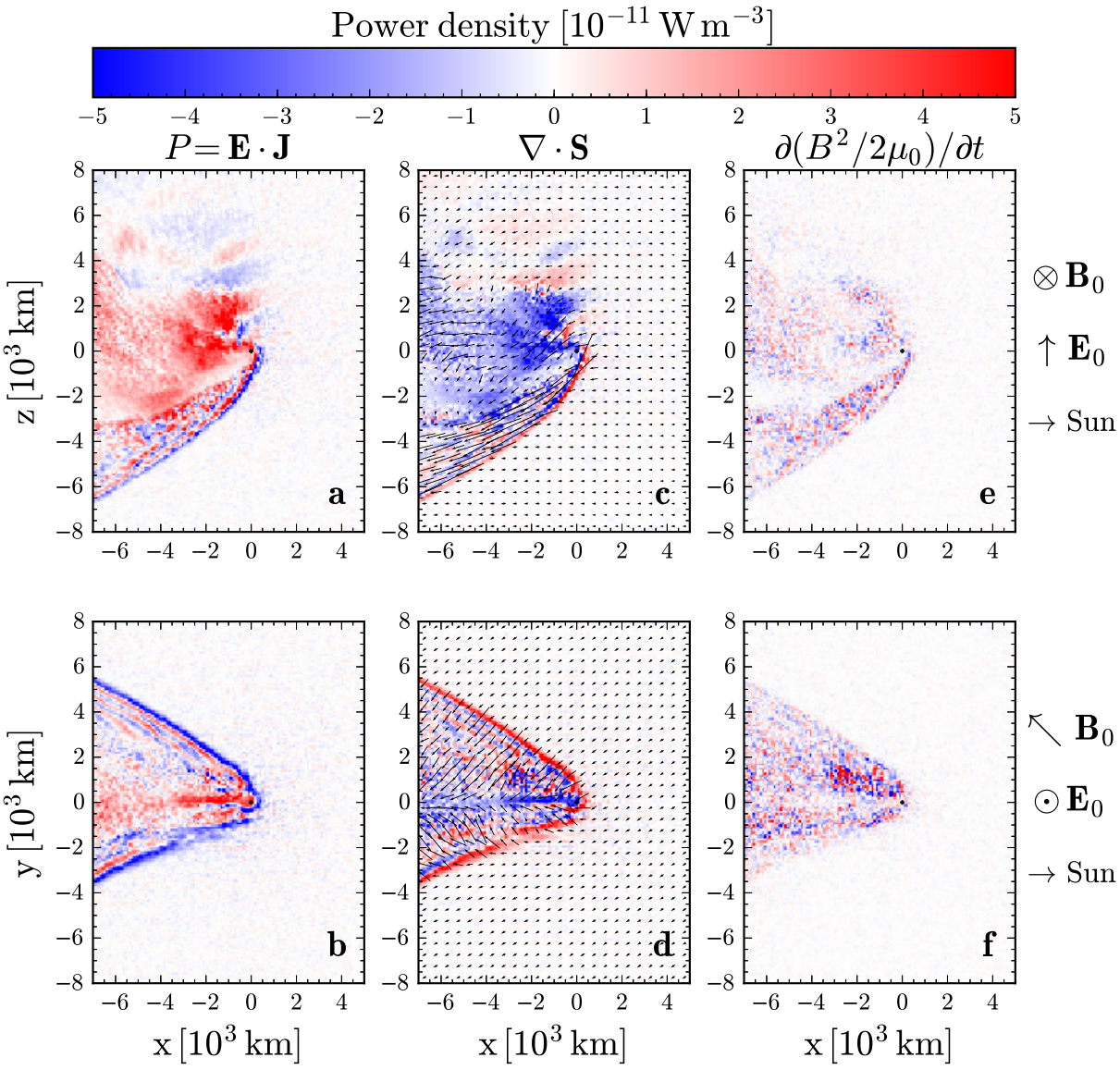


**Fig. 3.** Shown in color is the total power density (a, b), the divergence of the Poynting flux (c, d), and the time derivative of the electromagnetic energy density (e, f), for the $y = 0$ and $z = 0$ planes around the comet at 1.5 AU during weakly ionizing solar conditions. The Poynting theorem states that the sum of these three quantities should be zero for all points. The arrows in (c, d) mark the direction of the Poynting flux, $\mathbf{S} = \mathbf{E} \times \mathbf{B}/\mu_0$, and their sizes are proportional to the magnitude. The comet nucleus is marked by black crosshairs. The local geometry for each row of panels is shown to the right of the figure.

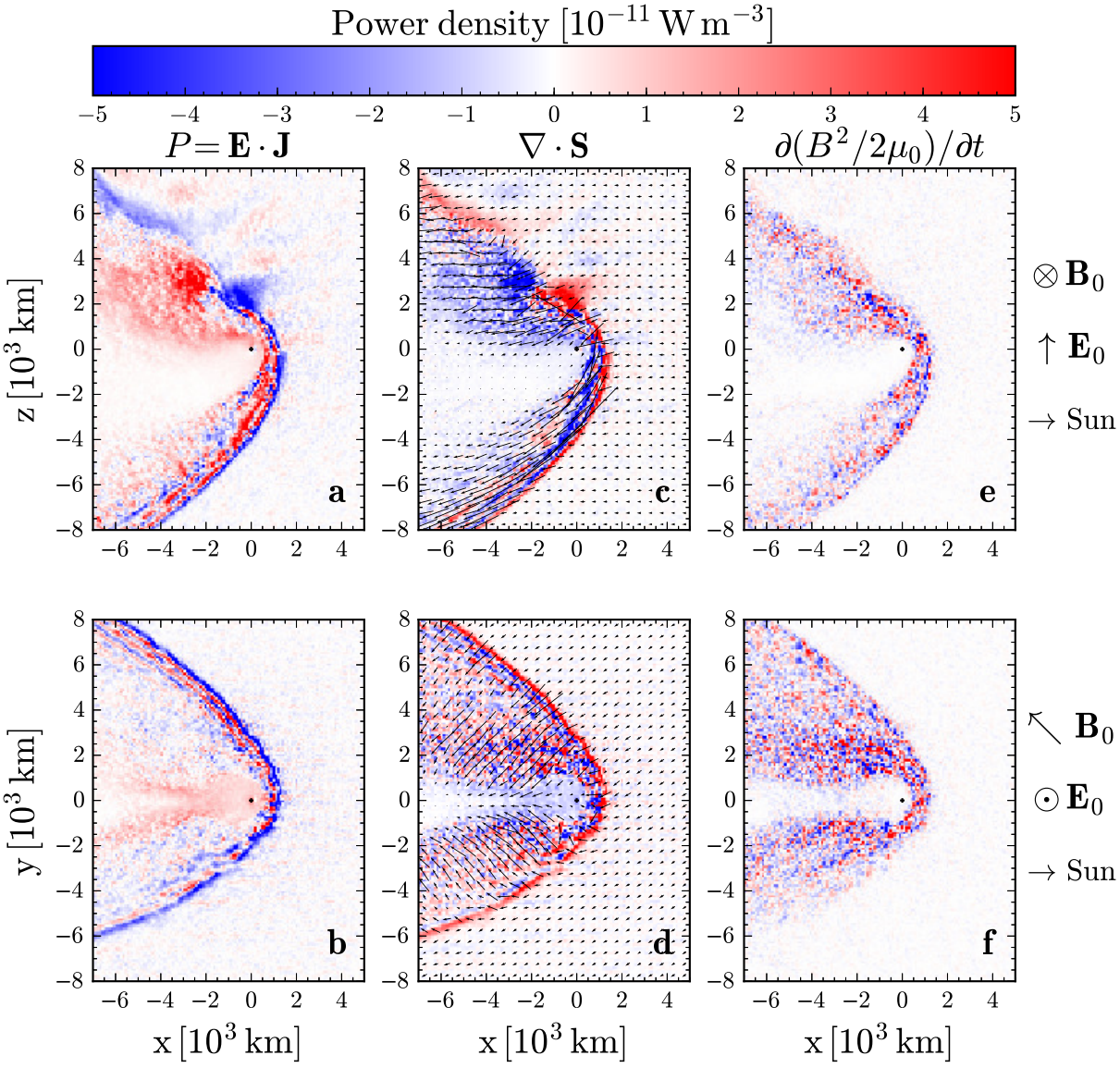


**Fig. 4.** Same form as Fig. 3 but for highly ionizing solar conditions.

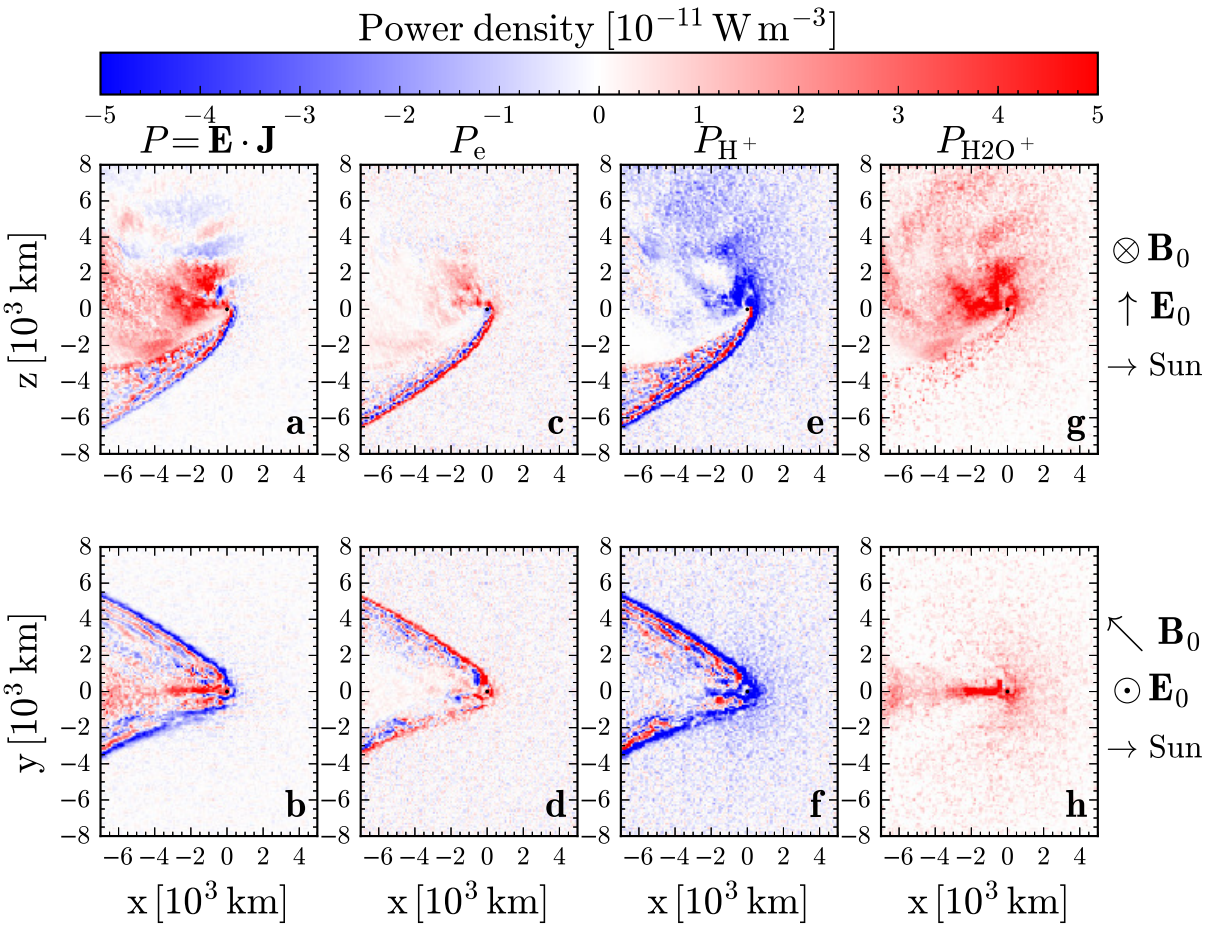


**Fig. 5.** Shown in color is the total power density (a, b), which is the sum of the electron power density (c,d), the solar wind proton power density (e, f), and the cometary water ion power density (g, h). Shown are cuts for the $y = 0$ and $z = 0$ planes around the comet at 1.5 AU during weakly ionizing solar conditions. Red ($\mathbf{E} \cdot \mathbf{J} > 0$) is where the electromagnetic field exerts work on charged particles, while blue ($\mathbf{E} \cdot \mathbf{J} < 0$) shows the opposite. The comet nucleus is marked by black crosshairs. The local geometry for each row of panels is shown to the right of the figure.

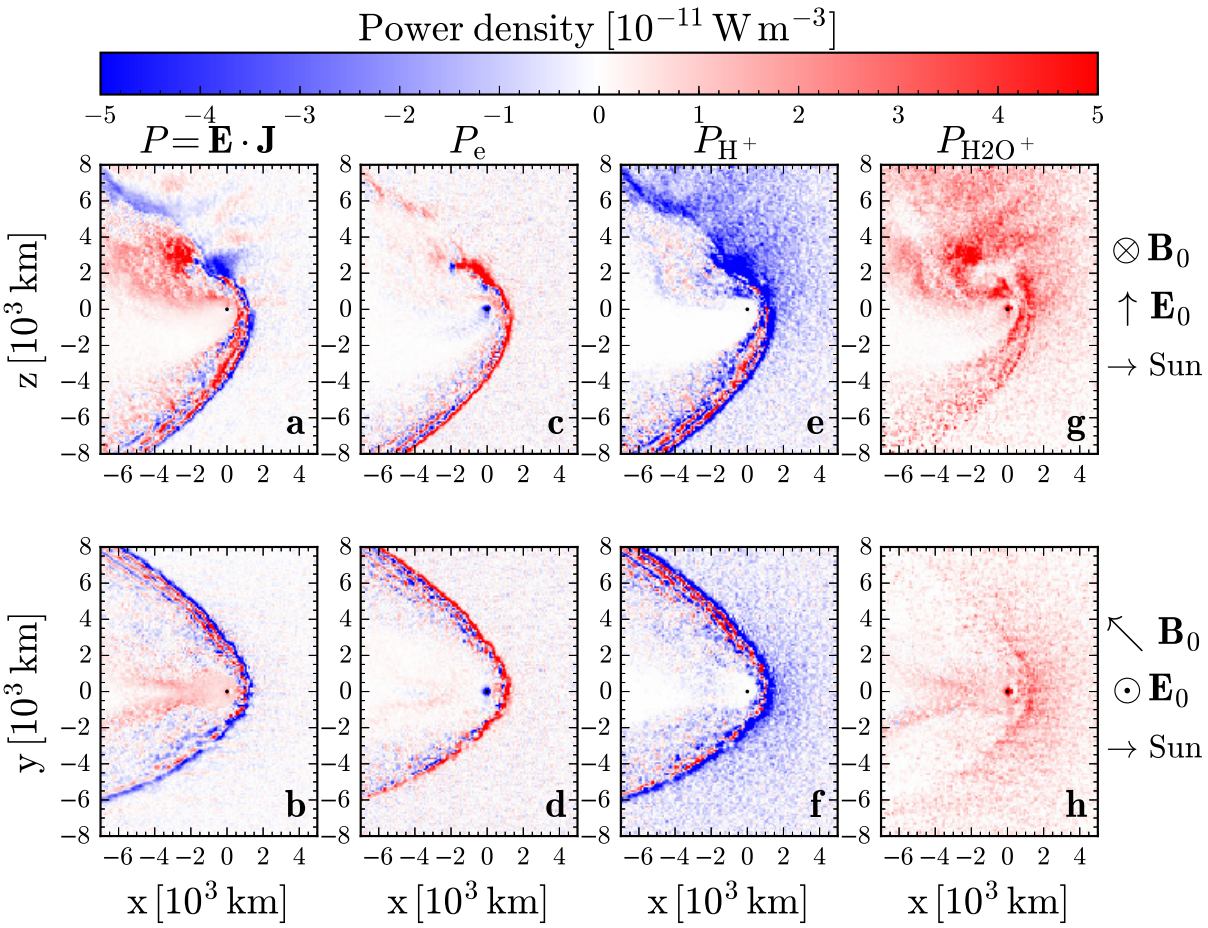


**Fig. 6.** Same form as Fig. 5 but for highly ionizing solar conditions.